Available online at www.sciencedirect.com

ScienceDirect

journal homepage: www.elsevier.com/locate/he

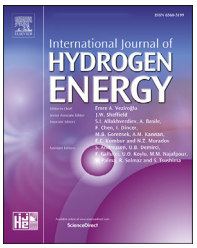

Strain rate and hydrogen effects on crack growth from a notch in a Fe-high-Mn steel containing 1.1 wt% solute carbon

Hina Najam [a,d], *Motomichi Koyama* [b], *Burak Bal* [c,*], *Eiji Akiyama* [b], *Kaneaki Tsuzaki* [a,e]

[a] *Department of Mechanical Engineering, Kyushu University, Motooka 744, Nishi-ku, Fukuoka 819-0395, Japan*
[b] *Institute for Materials Research, Tohoku University, Katahira 2-1-1, Aoba-ku, Sendai, Miyagi 980-8577, Japan*
[c] *Department of Mechanical Engineering, Abdullah Gül University, 38080 Kayseri, Turkey*
[d] *Department of Mechanical and Industrial Engineering, Ryerson University, Toronto, ON M5B 2K3, Canada*
[e] *HYDROGENIOUS, Kyushu University, Motooka 744, Nishi-ku, Fukuoka 819-0395, Japan*

HIGHLIGHTS

- Effects of strain rate and hydrogen on crack propagation from a notch are studied.
- Yield strength and elongation are degraded by hydrogen charging.
- Early crack initiation at the notch tip before apparent yielding is observed.
- Coexistence of several hydrogen embrittlement mechanisms are observed.

ARTICLE INFO

Article history:
Received 23 August 2019
Received in revised form
20 October 2019
Accepted 27 October 2019
Available online 27 November 2019

Keywords:
High-Mn steel
Intergranular crack
Crack propagation
Hydrogen embrittlement
Dynamic strain aging

ABSTRACT

Effects of strain rate and hydrogen on crack propagation from a notch were investigated using a Fe-33Mn-1.1C steel by tension tests conducted at a cross head displacement speeds of 10^{-2} and 10^{-4} mm/s. Decreasing cross head displacement speed reduced the elongation by promoting intergranular crack initiation at the notch tip, whereas the crack propagation path was unaffected by the strain rate. Intergranular cracking in the studied steel was mainly caused by plasticity-driven mechanism of dynamic strain aging (DSA) and plasticity-driven damage along grain boundaries. With the introduction of hydrogen, decrease in yield strength due to cracking at the notch tip before yielding as well as reduction in elongation were observed. Coexistence of several hydrogen embrittlement mechanisms, such as hydrogen enhanced decohesion (HEDE) and hydrogen enhanced localized plasticity (HELP) were observed at and further away from the notch tip resulting in hydrogen assisted intergranular fracture and cracking which was the key reason behind the ductility reduction.

* *Corresponding author.*
E-mail address: burak.bal@agu.edu.tr (B. Bal).
https://doi.org/10.1016/j.ijhydene.2019.10.227

Introduction

Among various austenitic steels, Fe–Mn–C based austenitic steels have received much attention over the past decade owing to their high work hardening capability [1] and associated excellent combination of tensile strength and ductility. These superior mechanical properties of Fe–Mn–C austenitic steels stem from a high strain-hardening rate associated with the presence of deformation twins, microstructural interactions during deformation [2,3] and the occurrence of dynamic strain aging (DSA) [4–6]. In addition, the stable face-centered cubic (FCC) structure at room temperature in the Fe–Mn–C austenitic steels has also been noted because of the low hydrogen diffusion coefficient compared with that of body-centered cubic structure in steels [7,8]. Since the low hydrogen diffusivity has been recognized to be key to developing hydrogen-resistant steel [9,10], the Fe–Mn–C austenitic steels are also candidate materials for the usage in hydrogen-related infrastructures [11,12]. However, they have been reported to undergo hydrogen embrittlement (HE) after significant plastic deformation with significant hydrogen content [13,14].

Even though HE is well-acknowledged failure mechanism especially in high strength steels the exact mechanisms of it is still unclear. The HE susceptibility of Fe–Mn–C steels has been studied by many researchers across the globe under various types of loading conditions [15–18]. Among several proposed HE mechanisms, hydrogen enhanced decohesion (HEDE), hydrogen induced localized plasticity (HELP) and adsorption induced dislocation emission (AIDE) are the most widely observed HE mechanisms in Fe–Mn–C austenitic steels [19–22]. A key point to understand the exact HE mechanism of the Fe–Mn–C austenitic steels is that the HE occurs after significant plastic deformation unlike martensitic steels. During the plastic deformation, various types of deformation microstructures evolve, e.g., increasing dislocation density, dislocation cell formation, and deformation twinning. The plasticity-induced microstructure evolution causes heterogeneities of lattice defect and hydrogen distributions, which trigger hydrogen-assisted cracking [23,24]. However, deformation microstructure evolution in the Fe–Mn–C steels is strongly dependent on chemical composition, because of the variations of dislocation-solute interaction [25–27] and stacking fault energy (SFE) [2,3,28]. Therefore, the Fe–Mn–C based austenitic steels show variety in HE behavior, depending on alloying elements and their content [15]. The effect of alloying elements such as nickel, aluminum and carbon on the HE susceptibility of austenitic steels has also been studied [29–31]. Among the alloying elements, carbon has been known to have a remarkable effect on the HE resistance as it affects deformation microstructure evolution associated with carbon-dislocation interaction and a significant increase in SFE [32,33]. More specifically, even without hydrogen, solute carbon causes deterioration in the ductility when the SFE and carbon content are relatively high [33]. This negative carbon effect is associated with DSA-induced localized plasticity, which appears remarkably when SFE-driven work hardening capability is low [33]. The carbon effect can co-act with the detrimental hydrogen effect [34].

The co-effect of hydrogen and carbon on the tensile behavior of Fe–Mn–C steels with a relatively high SFE, e.g., Fe-33Mn-1.1C, has been investigated in terms of crack initiation [33]. For instance, it has been reported that in hydrogen charged specimens, three crack initiation sites were observed in the Fe-33Mn-1.1C steel: grain boundary, twin boundary, and cell wall [15,35]; particularly, the cell wall cracking is a characteristic phenomenon, which has not been observed in low SFE Fe–Mn–C steels. Apart from the crack initiation, crack propagation behavior in the presence of hydrogen has been recently investigated [24,36]. Interestingly, a portion of the crack propagation path is transgranular and not along {111} twin/slip planes, which is also considered to arise from DSA-induced plastic strain localization [37–39]. However, crack propagation behavior from a notch of Fe–Mn–C austenitic steels in the presence of hydrogen at different strain rates has not been investigated yet. The crack propagation mechanism is practically important because crack propagation behavior becomes a predominant process for failure when the steels are applied to actual structural components that contain significant stress concentration sources, where crack initiation rather easily occurs.

In the present study, the effects of strain rate and hydrogen on crack propagation path from a notch in Fe-33Mn-1.1C steel have been investigated. For this purpose, tensile tests have been carried out on notched specimens with and without hydrogen at two different initial strain rates. Furthermore, the corresponding microstructure has been characterized to understand the underlying mechanisms of the crack propagation.

Experimental procedure

Material

An Fe-33Mn-1.1C (in mass%) ingot was prepared by vacuum induction melting furnace. The ingot was forged and rolled down to 20 mm at 1273 K. It was then solution treated at 1273 K for 1 h followed by water quenching to suppress the formation of carbides. The detailed chemical composition of the specimen is listed in Table 1. The average grain size was measured to be 33 μm including the annealing twin boundaries.

Tensile test specimens with the gauge length of 10 mm, width of 10 mm, and thickness of 1 mm were cut from the bar by using electro-discharge machining (EDM). Chemical polishing was done on the specimen surface using a mixture of 2 ml 55% HF and 18 ml H_2O_2 to remove the EDM layer. A 1 mm through-all drill hole was introduced at the center of the gauge length by micro drilling. A notch passing through the drill hole was introduced perpendicular to the loading direction in the

Table 1 – Chemical composition of the steel used (in mass %).

C	Si	Mn	P	S	Cu	Fe
1.12	0.03	32.6	<0.01	0.01	<0.002	Balance

specimen using EDM with a total notch length of 3 mm and notch thickness of 0.2 mm, which is the diameter of the EDM wire. The detailed geometry of the specimen is shown in Fig. 1.

Crack propagation experiment

Tensile tests were conducted at 303 K in air and in hydrogen environment. First, the tensile tests were carried out at cross head displacement speeds of 10^{-2} and 10^{-4} mm/s in order to investigate the effects of DSA due to carbon on the crack propagation solely. Then, the hydrogen effect was examined by conducting the tests at an identical cross head displacement speed of 10^{-4} mm/s under hydrogen charging. Before the tensile tests, both sides of the specimen surface were mechanically polished to remove scratches and corrosion layers that can form during the notching process. Hydrogen was introduced into the specimen during the tensile test by in-situ electrochemical charging in a 3% NaCl aqueous solution containing 3 g/L NH_4SCN at a current density of 10 A/m^2. A platinum wire was used as a counter electrode. The schematic outline of the equipment used for the hydrogen charging is shown in Fig. 2. During the tests carried out in air a video camera was used to observe the crack initiation and propagation from the notch. All the tensile tests were carried out until fracture, and once for each condition.

Microstructure characterization

The fracture surface of the specimen was observed by scanning electron microscope (SEM). Crystallographic features, dislocation pattern and crack propagation path was observed by electron backscatter diffraction (EBSD) and electron channeling contrast imaging (ECCI). The EBSD and ECCI were operated at accelerating voltages of 20 and 30 kV, respectively. The specimens for EBSD and ECCI were mechanically polished using colloidal silica with a particle size of 60 nm. The thickness reduction after mechanical polishing was less than 25%.

Finite element analysis

The hydrostatic stress with distance from the notch was simulated using the commercial finite element analysis (FEA) software ABAQUS. The tensile data for the smooth Fe-33Mn-1.1C specimen tensile tested at cross head displacement speed of 10^{-4} and 10^{-2} mm/s in air [34] was used for the hydrostatic stress simulation. A 3D deformable part was defined in Abaqus with linear hexahedral mesh elements with type C3D8R. Elasto-Plastic material model, that assumes isotropic hardening, were used and a ductile damage criterion was used as a failure mechanism. The initial stress triaxiality value was taken as 0.33 which is known to be the standard value under uniaxial tensile load [40]. Due to the symmetry of the specimen, half of the specimen was simulated for reduced computation time. One end of the specimen was fixed while uniform velocity boundary condition was applied at the other end. The uniform instantaneous velocities for the specimen tensile tested at cross head displacement speeds 10^{-4} and 10^{-2} mm/s in air were taken as 10^{-4} and 10^{-2} mm/s, respectively. Extremely fine meshing with minimum mesh volume of 2.491×10^{-14} mm^3 was generated near the notched region in order to observe the variation of hydrostatic stress near the notch tip. The tensile tests were simulated until yield. The yield point was determined by the stress along the tensile direction and corresponding plastic strain values at a particular nodal point in the center of the specimen. The values for yield strength were found to be 388.5 and 378.6 MPa for specimens tensile tested at cross head displacement speeds of 10^{-4} and 10^{-2} mm/s. The corresponding remote displacement at yield for both the specimens was then found to be 0.0187 mm and 0.0156 mm, respectively. The variation of hydrostatic stress with distance from the notch for the specimens was then plotted at the defined cross head displacement speeds. The hydrostatic stress was obtained from the pressure distribution on the specimen at yield for different cross head displacement speeds using the relation where pressure equals the negative of the hydrostatic stress.

Results

Crack propagation: tensile test results

Fig. 3 shows engineering stress vs. displacement curves at cross head displacement speeds of 10^{-2} and 10^{-4} mm/s in air and at cross head displacement speed of 10^{-4} mm/s under hydrogen charging. The serrated flow indicates occurrence of DSA which was suppressed by hydrogen charging [30,36]. Decreasing cross head displacement reduced the elongation by 11%. The hydrogen charging deteriorated the elongation by 32% as well as the work hardening ability. A significant finding was that hydrogen reduced the yield strength (determined by 0.2% proof stress method from the engineering stress and calculated mean engineering strain) of the material by 40% from 423 MPa to 253 MPa. This is in opposition to the previous studies on TWIP steels where hydrogen either increases the yield strength of the material or has no significant effect on it, demonstrating that the presence of notch has a significant

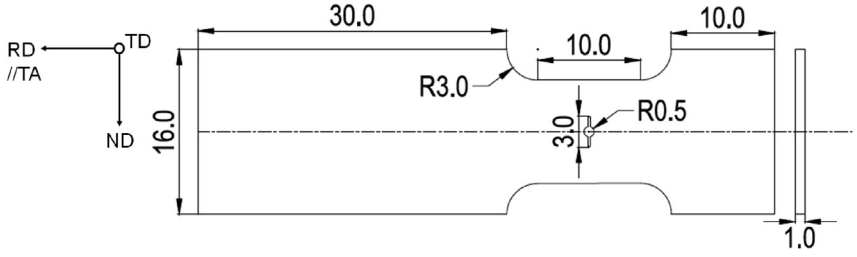

Fig. 1 – Specimen geometry used for the present study (mm).

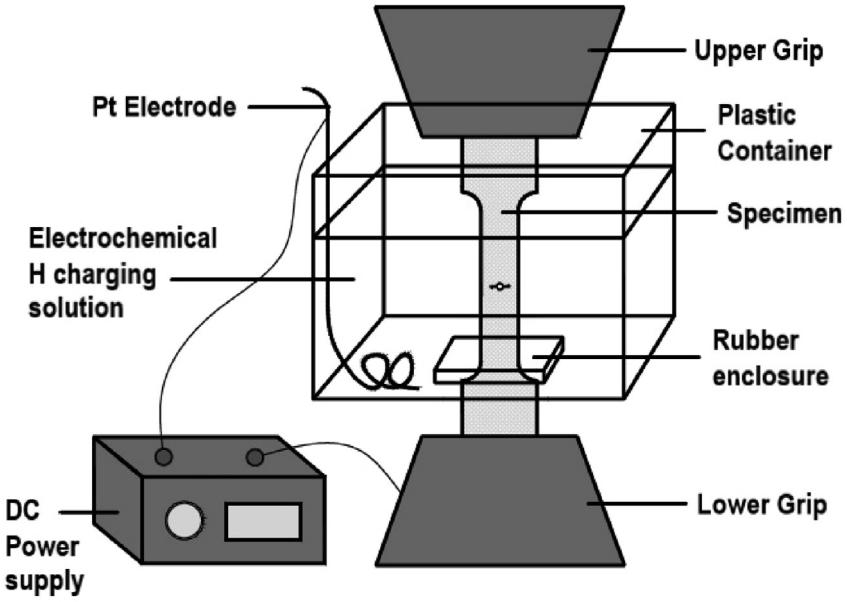

Fig. 2 – Schematic outline of the equipment used for the hydrogen charging.

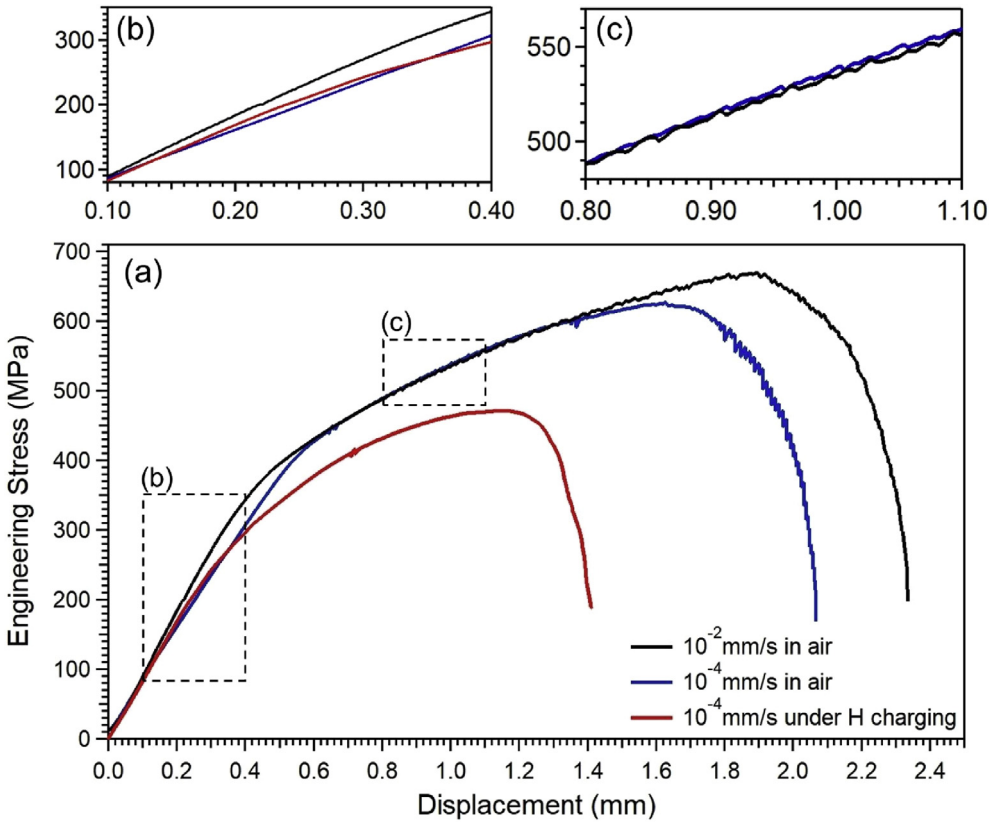

Fig. 3 – (a) Engineering stress vs displacement curve at cross head displacement speed of 10^{-2} and 10^{-4} mm/s in air, and cross head displacement speed of 10^{-4} mm/s under hydrogen charging. (b, c) Magnifications of the highlighted portion of (a).

effect on the tensile behavior of the steel [14,33]. After the ultimate tensile stress (UTS), a significant drop in the stress level is seen in all three specimens. The video observation indicated that the stress drop corresponded to unstable crack propagation.

Fig. 4 shows the crack growth behavior captured by video imaging for the tensile tests carried out in air at cross head displacement speeds of 10^{-2} and 10^{-4} mm/s. From the video images, crack length was measured as a projected crack length. The crack length vs. displacement curves at cross head

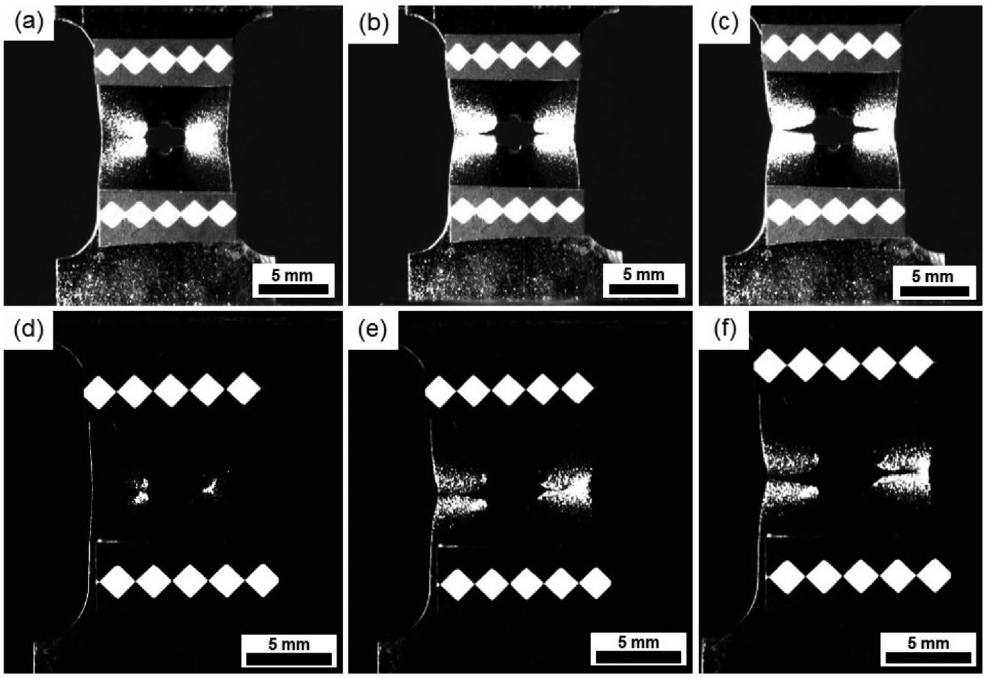

Fig. 4 – (a, b, c) - Video images of the specimen taken at 10^{-2} mm/s in air at stroke values of (a) 2.07, (b) 2.27, and (c) 2.32 mm (d, e, f) Video images of the specimen taken at 10^{-4} mm/s in air at stroke values of (d) 1.50, (e) 2.03, (f) 2.07 mm.

displacement speeds of 10^{-2} and 10^{-4} mm/s in air are shown in Fig. 5. Here the crack length is defined as the distance between two crack tips. From Fig. 5, it can be seen that a crack initiated at smaller displacement at the lower cross head displacement speed compared with at the higher cross head displacement speed. Initially stable crack growth occurred in both specimens followed by unstable crack growth which was observed by the drastic increase in the crack length with increasing cross head displacement. In Fig. 6, the crack length is plotted against the engineering stress. The early stage of the crack propagation at 10^{-4} mm/s in air (until the fifth data point) shows peculiar behavior, namely, the stress level is higher than those at 10^{-2} mm/s and in the late stage at 10^{-4} mm/s. This is because, the early crack propagation stage at 10^{-4} mm/s corresponds to the deformation stage before reaching the UTS or immediately after the UTS, which indicates that work hardening of the ligament still controls the engineering stress in the early crack propagation stage. In contrast, when the crack propagates after the UTS, a drastic reduction in stress level was observed, namely, the primary factor altering the engineering stress in the late stage is crack propagation. The crack propagation behaviors at the two displacement speeds in the late stage show almost the same

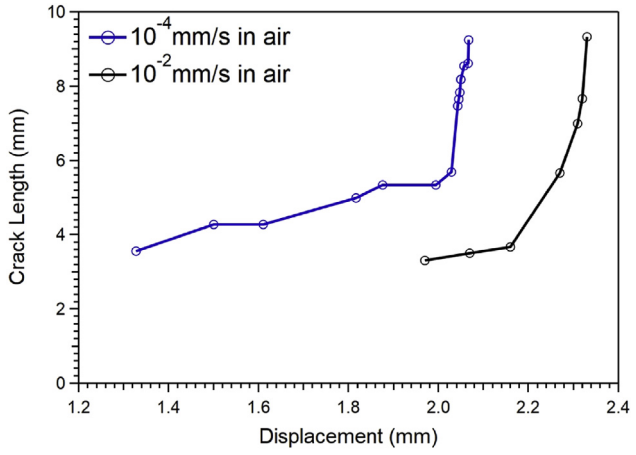

Fig. 5 – Crack length vs. Displacement curve at cross head displacement speeds of 10^{-2} mm/s, and 10^{-4} mm/s in air. Note that the initial crack (notch) length is 3 mm and the specimen width is 10 mm.

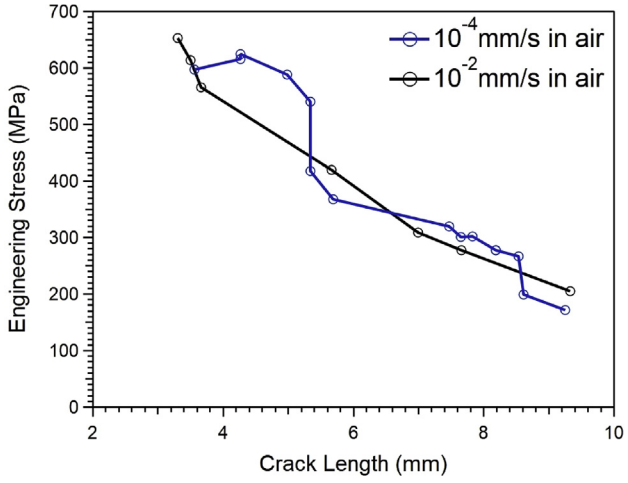

Fig. 6 – Engineering stress vs. Crack length curve at cross head displacement speed of 10^{-2}, and 10^{-4} mm/s in air. Note that the initial crack length is 3 mm and the specimen width is 10 mm.

stress dependence. This fact indicates that crack propagation is entirely stress dependent, irrespective displacement speed.

Fractrographic feature

The fracture surface of the specimen fractured at 10^{-4} mm/s in air is shown in Fig. 7. From Fig. 7(b) and (c), intergranular fracture near the notch can be seen with significant amount of slip traces indicating plasticity driven intergranular cracking. Quasi-cleavage features were also observed as indicated by the yellow arrows. Far from the notch in Fig. 7 (d) and (f) and their magnified images, dimples were observed. Numerous subcracks throughout the fracture surface were observed as shown in Fig. 7. Fig. 8 shows the fracture surface of the specimen obtained by the test at 10^{-2} mm/s in air. With increasing cross head displacement speed, the fracture mode near the notch, as shown in Fig. 8 (b) and (c), changed from brittle intergranular to ductile dimple like that had been formed by the coalescence of microvoids. Throughout the fracture surface, the fracture mode remained continuous as shown in Fig. 8 (d) and (f) and their magnified counterparts, indicating that with increasing cross head displacement speed, the presence of the notch had no significant effect on the fracture mode of the specimen. This is similar to the case for the smooth specimen where with increasing cross head speed, the fracture mode changes from brittle intergranular to ductile fracture surface with well-developed dimples throughout the entire fracture surface of the specimen [34].

The fracture surface of the specimen obtained by the test at 10^{-4} mm/s in hydrogen environment is shown in Fig. 9. In case of hydrogen charged specimen, close to the notch, smooth brittle intergranular fracture was observed as shown in Fig. 9(b and c). Existing probability of quasi-cleavage feature was increased by hydrogen charging as seen in Fig. 9(c) and (e), but the main fracture mode remained intergranular. However, at the mid thickness of the specimen, some ductile dimple-like fracture features were observed particularly when the crack length increased as shown in Fig. 9 (d, f, g), which might be the result of hydrogen diffusion problem. As hydrogen charging was conducted during the tensile test, hydrogen did not have enough time to diffuse through the center of the specimen from the side surfaces and the crack surface at the large crack length (the crack growth rate is high), which thereby could not affect the deformation mode.

Microstructures beneath the fracture surface

The EBSD RD-IPF map and the reference grade orientation deviation (GROD) map of the specimen fractured at 10^{-4} mm/s in air are shown in Fig. 10. A considerable amount of deformation twinning activity can be observed in the grains underneath the fracture surface as shown by the RD-IPF map in Fig. 10 (b). From the GROD map in Fig. 10(c), a significant amount of plastic deformation can be observed resulting from high amount of localized microscopic plastic strain distribution. Fig. 11 shows the EBSD RD-IPF map and the GROD map of the specimen fractured at 10^{-2} mm/s in air. Similar to the specimen fractured at 10^{-4} mm/s in air, significant amount of plastic deformation and twinning activity was observed in the specimen tensile tested at higher cross head displacement speed as shown in Fig. 11(b and c).

Fig. 12 shows the EBSD RD-IPF and GROD map for the specimen fractured at 10^{-4} mm/s under hydrogen charging. With the introduction of hydrogen, significant reduction in

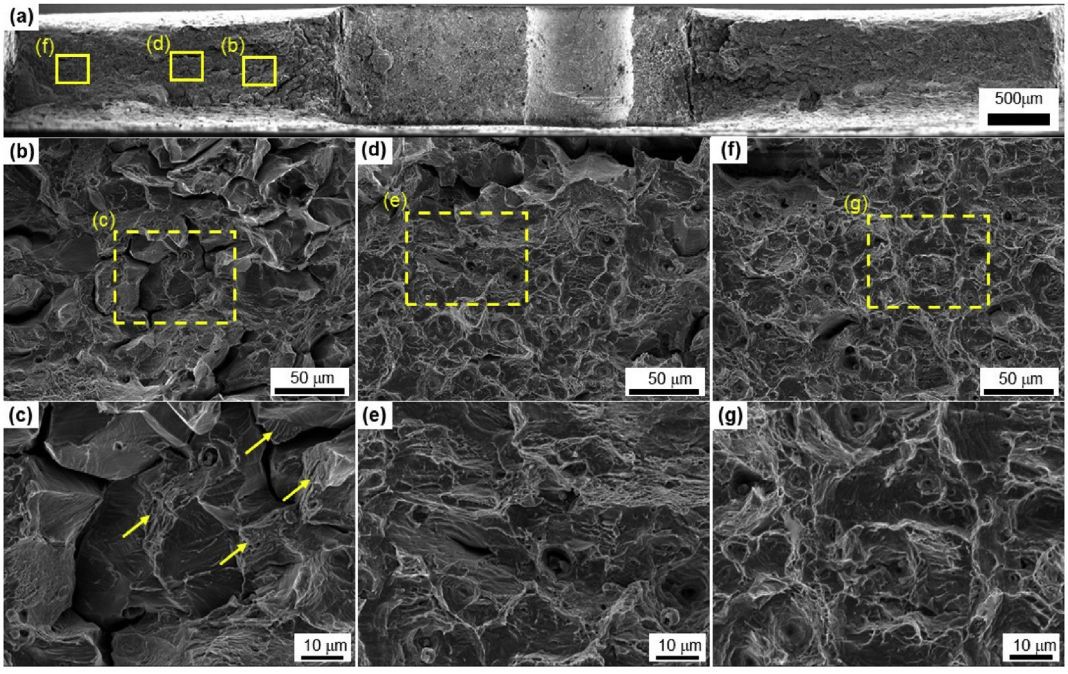

Fig. 7 – (a) An overview of the fracture surface obtained by the test at 10^{-4} mm/s in air. Magnified images (b, c) near notch tip, (d, e) in the middle part, and (f, g) near the final fracture region. Note that the position of the drill hole is not located in the center of the specimen as seen in (a); however, the center of the notch is located at the center of the specimen width. Therefore, the mechanical condition of this specimen is approximately equivalent to the other specimens.

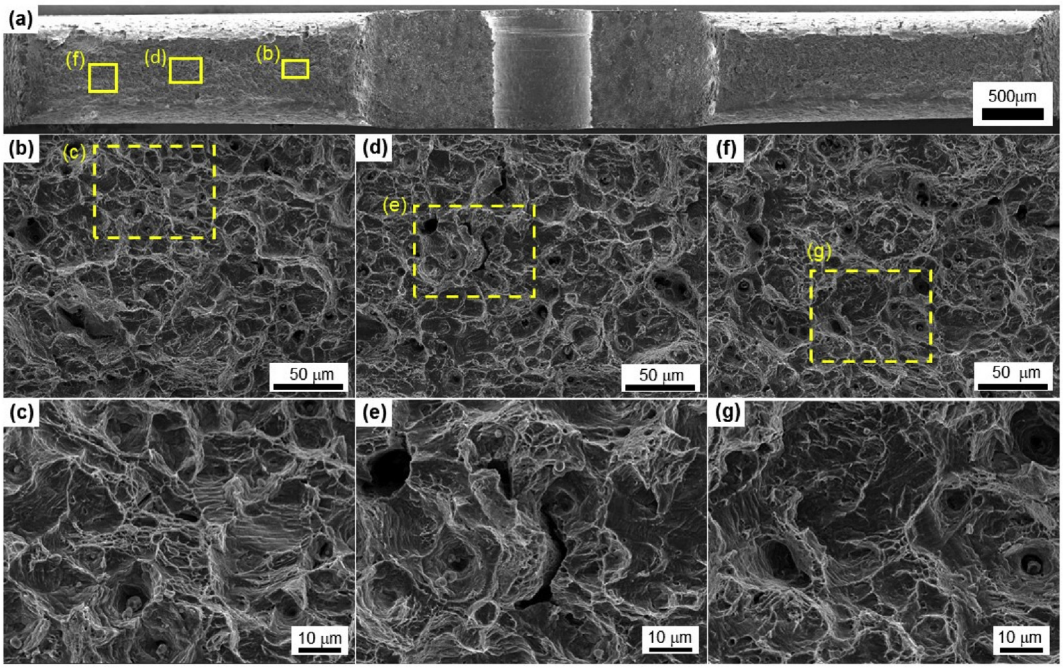

Fig. 8 – (a) An overview of the fracture surface obtained by the test at 10^{-2} mm/s in air. Magnified images (b, c) near notch tip, (d, e) in the middle part, and (f, g) near the final fracture region.

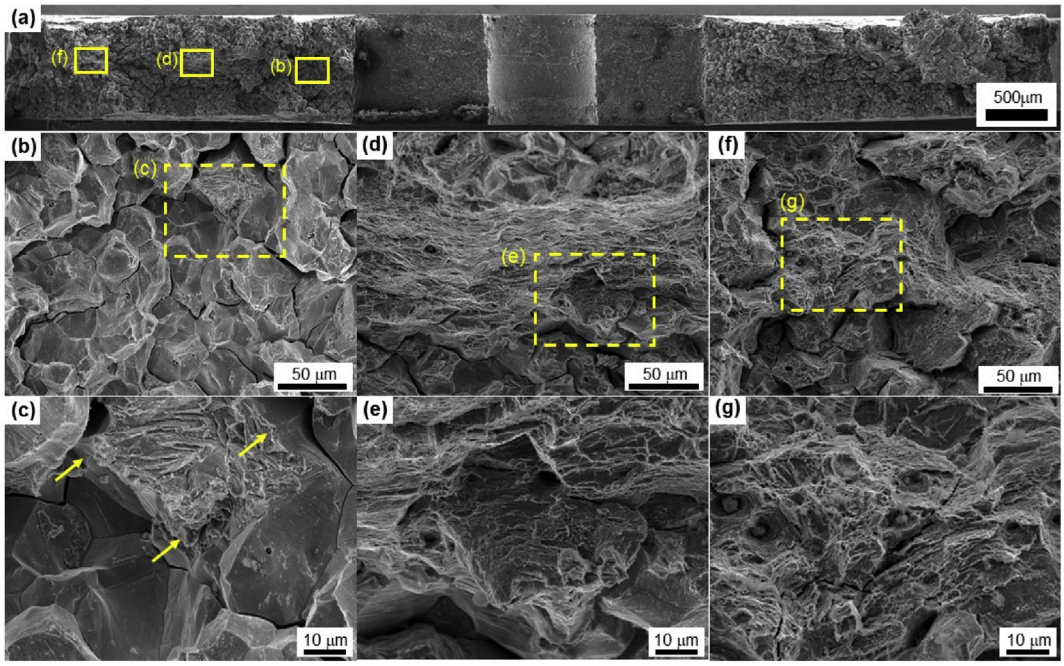

Fig. 9 – (a) An overview of the fracture surface obtained by the test at 10^{-4} mm/s in hydrogen environment. Magnified images (b, c) near notch tip, (d, e) in the middle part, and (f, g) near the final fracture region. The yellow arrows in (c) indicate quasi-cleavage fracture region. (For interpretation of the references to color in this figure legend, the reader is referred to the Web version of this article.)

the amount of twinning activity can be observed in the grains underneath the fracture surface as shown by the EBSD RD-IPF map in Fig. 12 (b). This is unlike the case for the smooth specimen where considerable amount of twinning activity has known to be observed in the grains underneath the fracture surface but far below the fracture surface, the twinning activity has known to reduce contributing to localized plasticity near the fracture edge for the hydrogen charged specimen [33]. Most of the grains in our present study show considerably less plastic strain distribution as indicated by the GROD map

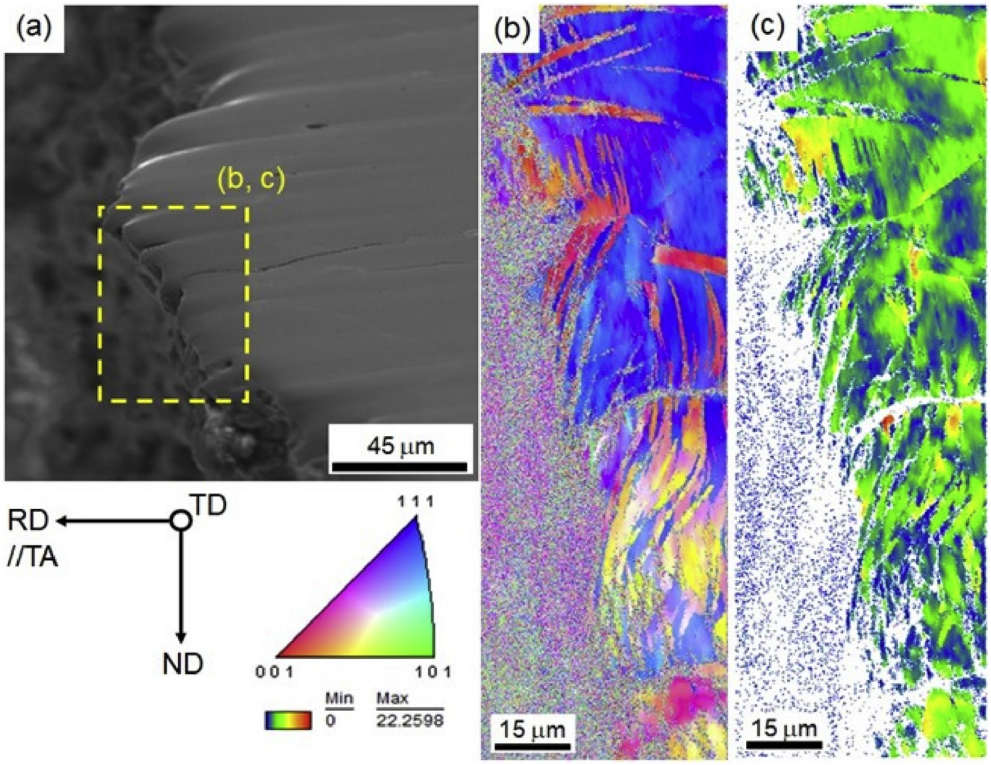

Fig. 10 – (a) SE image, (b) RD-IPF map, and (c) GROD map of the specimen fractured at 10^{-4} mm/s in air.

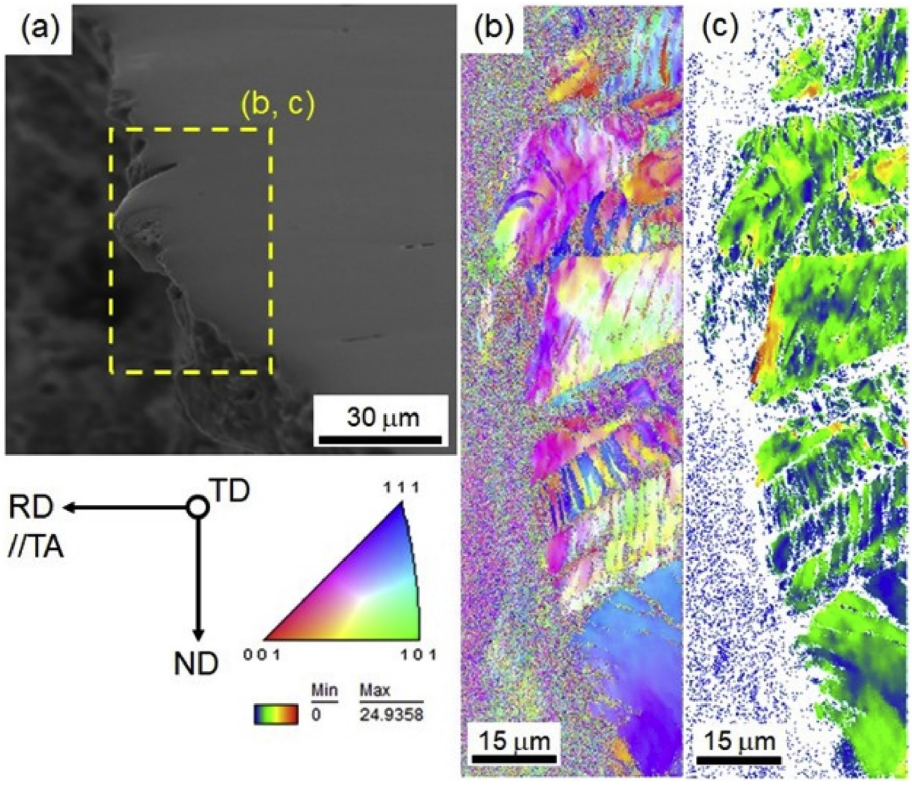

Fig. 11 – (a) SE image, (b) RD-IPF map, and (c) GROD map of the specimen fractured at 10^{-2} mm/s in air.

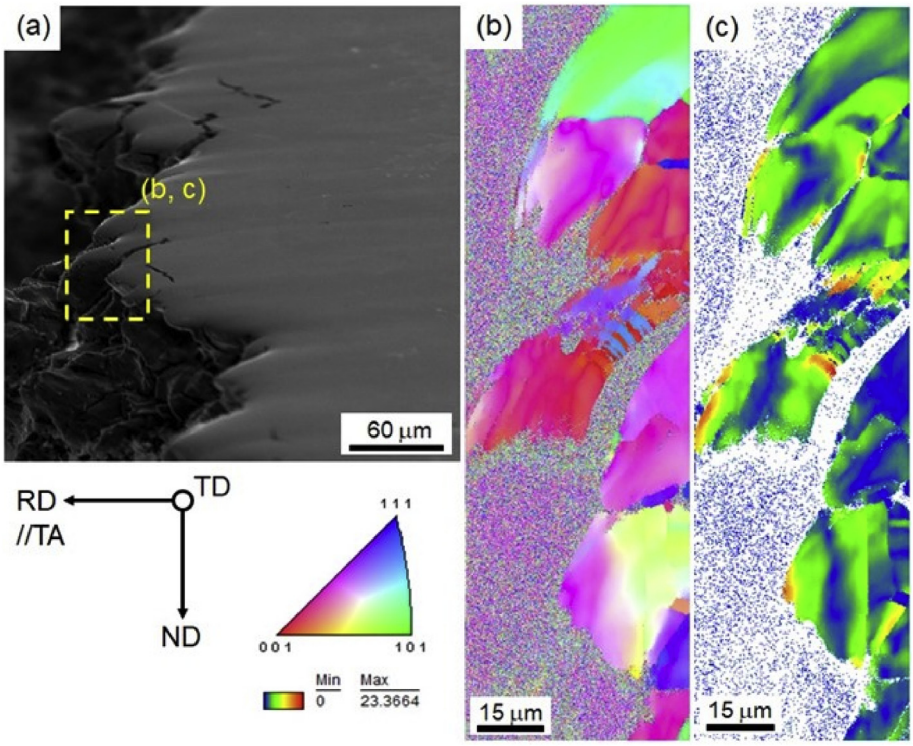

Fig. 12 – (a) SE image, (b) RD-IPF map, and (c) GROD map of the specimen fractured at 10^{-4} mm/s under hydrogen charging.

in Fig. 12 (c). However, a significant amount of strain localization is observed in the grains underneath the fracture surface in hydrogen charged specimen as seen by the lower GROD value in Fig. 12 (c) compared with Fig. 10 (c). This result is similar to the uncharged specimen contributing to localized plasticity.

The ECC image close to the fracture surface obtained by the test at 10^{-4} mm/s in air is shown in Fig. 13 (a). Numerous subcracks were observed near the specimen fracture surface. Close to the notch, crack tip blunting was observed as shown in Fig. 13 (b). A significant amount of deformation twinning activity can be observed near the fracture surface with a dislocation-cell-like pattern formed between the twins indicated by Fig. 13(b–g). Fig. 14 shows the ECC image close to the fracture surface obtained by the test at 10^{-2} mm/s in air. In the case of higher cross head displacement speed, reduced amount of subcracks can be observed close to the specimen fracture surface as shown in Fig. 14 (a). Similar to lower cross head displacement speed, at higher cross head displacement speed, a significant amount of deformation twinning activity can be observed with some dislocation pattern in between the twins as indicated by Fig. 14(b–g). Main failure occurred by ductile dimples (Fig. 8) but subcracks propagated along the grain boundaries in both specimens.

The ECC image close to the fracture surface obtained by the test at 10^{-4} mm/s under hydrogen charging is shown in Fig. 15. In the case of hydrogen charged specimen, intergranular cracking was observed near the notch as indicated by the ECC image in Fig. 15 (b). Numerous subcracks were observed close to the specimen fracture surface some of which are parallel to the fracture surface while some are orientated at an angle unlike the case for the uncharged specimen where subcracks parallel to the fracture surface were not observed. The propagation of the subcracks for the hydrogen-charged specimen was mainly along the grain boundary with sharp crack tips. Close to the fracture surface reduced amount of twinning activity was observed as shown in Fig. 15(b–g).

Stress distribution

The hydrostatic stress gradient with distance from the notch at yield for specimens tensile tested at 10^{-4} mm/s and 10^{-2} mm/s is shown in Fig. 16. Fig. 17 shows the pressure distribution at yield from where the hydrostatic stress for the specimens was obtained. From Fig. 16, it can be observed that the hydrostatic stress decreases with distance from the notch. For the specimen tensile tested at 10^{-4} mm/s, the hydrostatic stress at the notch tip is the highest compared to the one tensile tested at 10^{-2} mm/s. With increasing distance from the notch tip, the same drop in hydrostatic stress was observed in both specimens.

Discussion

Carbon-affected strain rate dependence

The first fact we note is the deterioration of elongation by decreasing the cross head displacement speed from 10^{-2} to 10^{-4} mm/s without hydrogen charging (Fig. 3). In this context, we found occurrence of intergranular crack initiation and small crack growth near the notch tip at 10^{-4} mm/s (observed as intergranular fracture surface in Fig. 7(b)), whereas the crack propagation path did not change with strain rate.

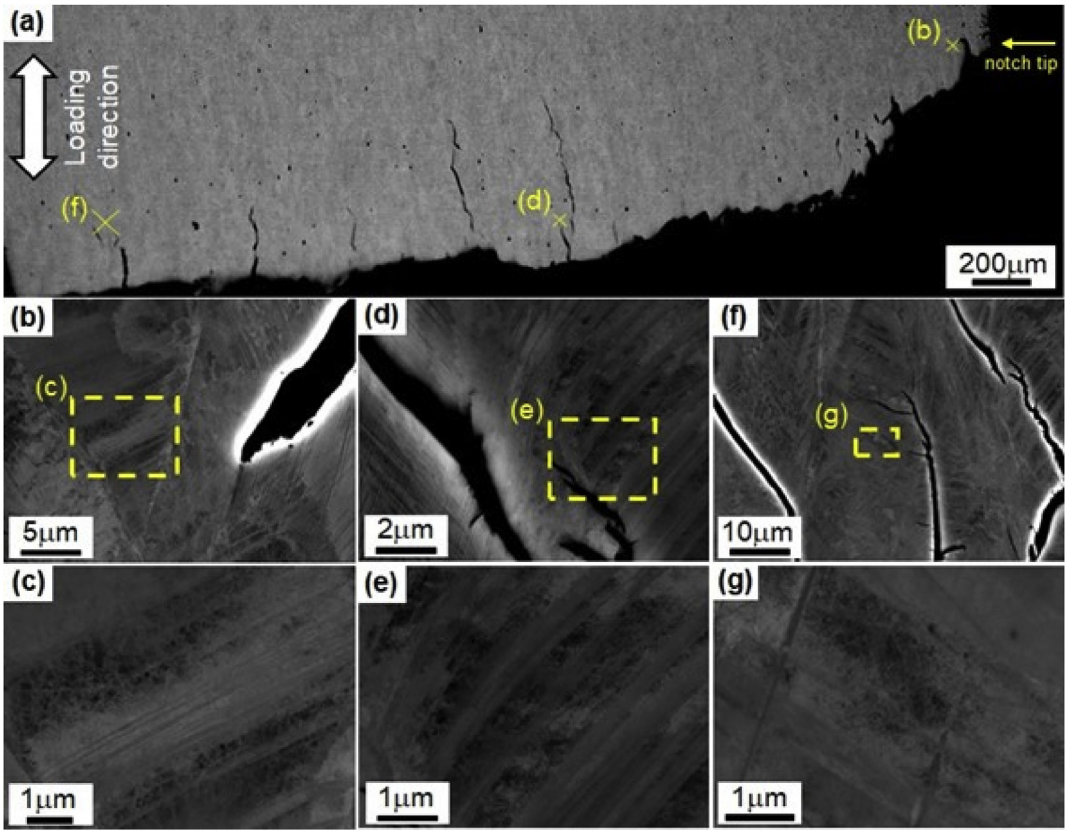

Fig. 13 – (a) ECC image close to the fracture surface obtained by the test at 10^{-4} mm/s in air. Magnified images (b, c) near notch tip, (d, e) in the middle part, and (f, g) near the end of specimen.

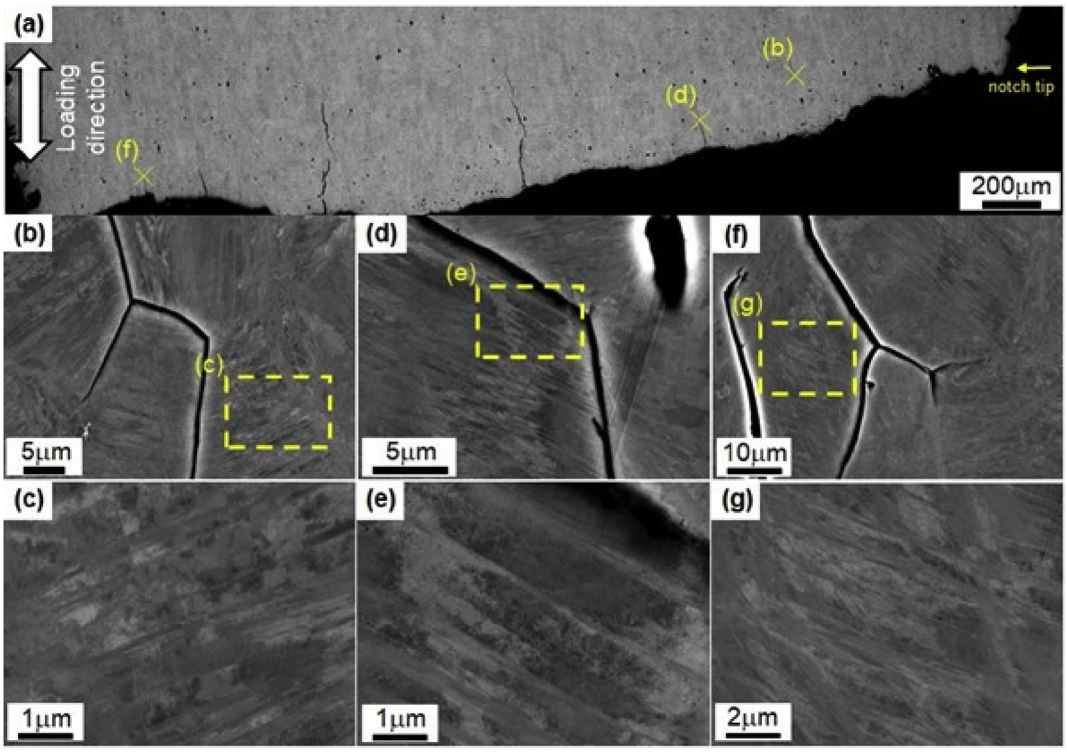

Fig. 14 – (a) ECC image close to the fracture surface obtained by the test at 10^{-2} mm/s in air. Magnified images (b, c) near notch tip, (d, e) in the middle part, and (f, g) near the end of specimen.

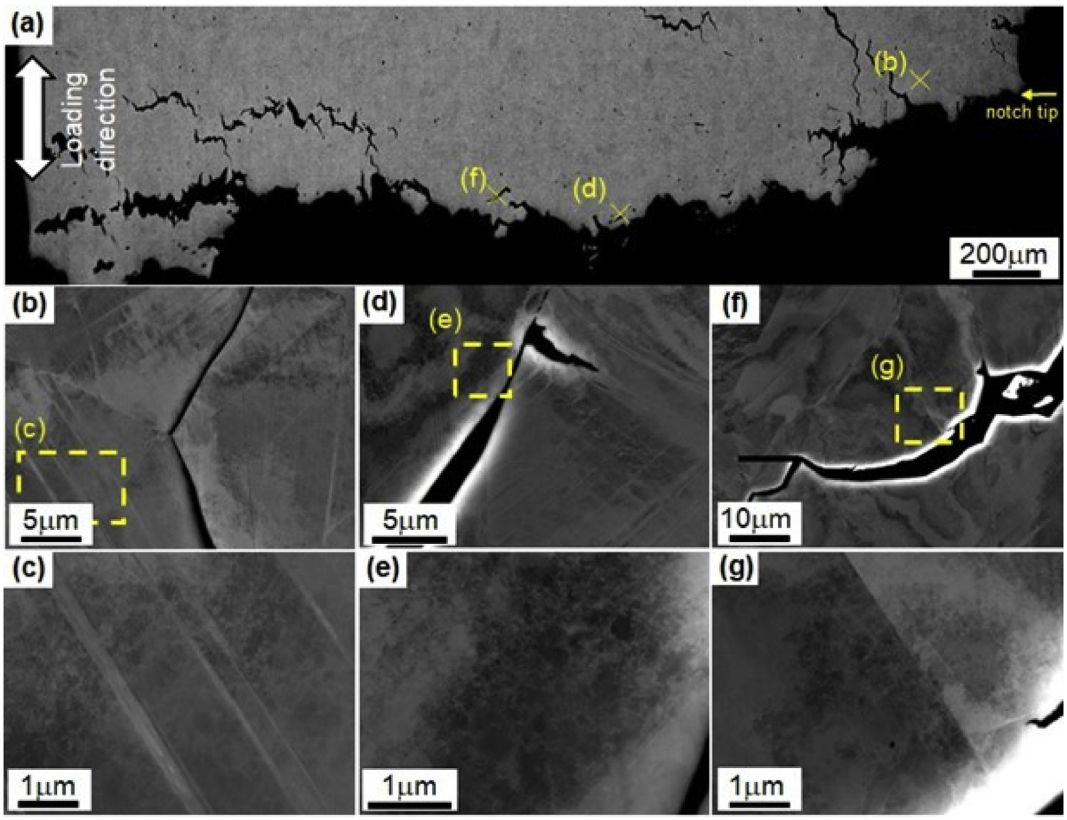

Fig. 15 – (a) ECC image close to the fracture surface obtained by the test at 10^{-4} mm/s under hydrogen charging. Magnified images (b, c) near notch tip, (d, e) in the middle part, and (f, g) a little away from the middle part.

Therefore, in order to explain the degradation in elongation by decreasing the cross head displacement speed, we note the occurrence of the intergranular cracking near the notch tip at 10^{-4} mm/s.

It is noteworthy that the cracking event on grain boundaries was suppressed with increasing crack length and strain rate (Figs. 7 and 8). If the intergranular cracking is a fully brittle event, which is controlled by only crack tip stress field, the intergranular cracking remains to occur with increasing crack length as long as the stress triaxiality at the crack tip is maintained. Also, the strain rate sensitivity of the intergranular cracking cannot be explained by simple dislocation mechanics, because local stress level, which increases with yield strength, increases with increasing strain rate owing to thermally activation process of dislocation motion. Therefore, we must consider another kinetic problem of plasticity-driven phenomenon to understand the intergranular cracking mechanism. In this regard, DSA, which has been confirmed to occur in the Fe-33Mn-1.1C steel [33,34], can be key to interpreting the cracking behavior. In general, the DSA in Fe–Mn–C austenitic steel is associated with solute carbon motion, which causes negative strain rate sensitivity of flow stress [41,42]. Specifically, lowering strain rate provides time for carbon motion, causing dislocation pinning and an associated increase in dislocation density [15,43]. The increase in dislocation density increases flow stress. Even before yielding, carbon interacts with pre-existing dislocation particularly under stress [44], which causes an increase in yield strength with decreasing strain rate. Accordingly, crack tip stress appears to be high at the yield stress when the deformation speed is low as shown in Figs. 16 and 17. After yielding, the difference in crack tip stress between the two deformation speed conditions further increases with decreasing strain rate because of the negative strain rate sensitivity of flow stress [45,46]. The high crack tip stress level associated with stress triaxiality and DSA-driven strengthening at the low strain rate assist to reach a critical strain energy for decohesion after

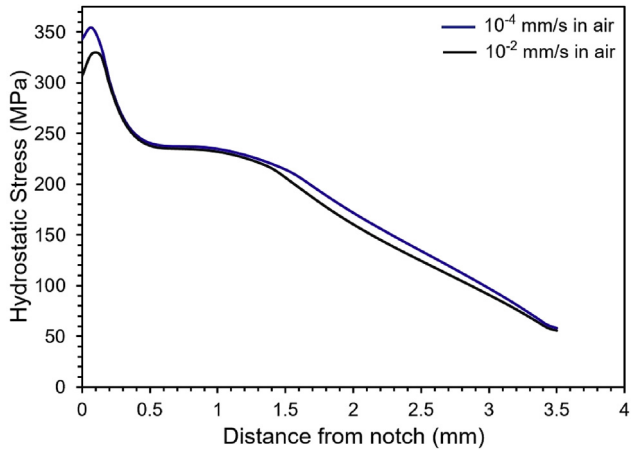

Fig. 16 – Hydrostatic stress vs distance from notch curves for specimens tensile tested at cross head displacement speed of 10^{-4} mm/s and 10^{-2} mm/s in air.

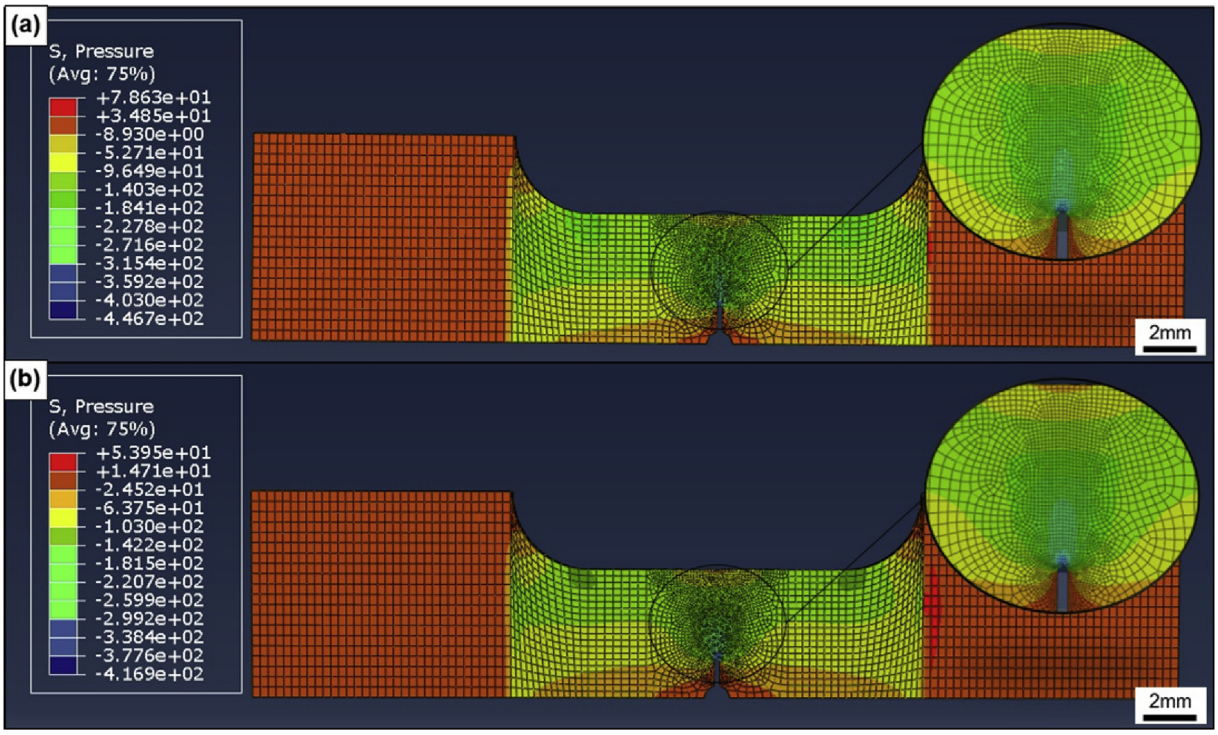

Fig. 17 – Pressure distribution at yield for specimen tensile tested at (a) 10^{-4} mm/s in air, and (b) 10^{-2} mm/s in air (Inset: Magnified images near the notched region).

yielding. Furthermore, the plasticity-driven damage causes microstructural boundary cracking such as grain boundary in Fe–Mn–C TWIP steels [37,47,48], which also occurred in the present case as indicated by the formation of slip traces on the intergranular fracture surface (Fig. 7). Therefore, the intergranular cracking at the notch tip can occur via the following process. (1) The dislocation-carbon interaction is enhanced by lowering deformation speed, which assists an increase in dislocation density and dislocation cell wall formation at the notch tip (Fig. 13(b and c)). (2) The dislocation microstructure evolution increases notch/crack tip stress, and the maximum stress is placed at a location slightly far from the notch tip as shown in Figs. 16 and 17. (3) Combined with plasticity-triggered damage along grain boundaries, intergranular cracking occurs at the location where stress is maximum.

In the process (1), hydrostatic stress gradient assists carbon diffusion, therefore, the carbon-dislocation effect appears to be significant particularly near the notch tip. Furthermore, in terms of mechanics, the stress triaxiality realize a high stress level that cannot appear in smooth specimen. Because of the two reasons, the intergranular cracking has not been observed as a primary phenomenon in smooth specimens [49]. Corresponding to the process (2), numerous subcracks were observed near the fracture surface at the cross-head speed of 10^{-4} mm/s (Fig. 13(a)), and its existing probability was decreased by increasing the cross-head speed to 10^{-2} mm/s (Fig. 14(a)). After the process (3), crack length increases, which increases local strain rate. The increase in local strain rate suppresses dislocation-carbon interaction such as DSA. Therefore, intergranular cracking was not observed in the long crack region as shown in Fig. 7(d–g). Since DSA effect does not occur at the long crack regime, a significant difference in dislocation microstructure between the specimens fractured at 10^{-2} and 10^{-4} mm/s was not observed in the middle and long crack length regions as shown in Figs. 13(d–g) and 14(d–g). Correspondingly, after the crack initiation regime, no significant change by varying deformation speed was observed (Fig. 5), and the growth behavior was controlled by mechanical condition, i.e. remote stress and crack length (Fig. 6).

Hydrogen effect

From a viewpoint of mechanical response, the hydrogen charging decreased yield strength and reduced the elongation (Fig. 3). The decrease in yield strength can be attributed to crack initiation at the notch tip before apparent yielding. As reported previously, cracking in the present steel charged with hydrogen easily occurs along grain boundaries, which causes a significant reduction in nominal flow stress even in smooth specimens via decreasing the cross sectional area [33,50]. Particularly in the specimen interior, similar to the case of carbon, the hydrostatic stress gradient in the plain strain condition causes hydrogen segregation at the notch tip, which accelerates occurrence of hydrogen-assisted cracking. Correspondingly, numerous subcracks were found around the notch tip as shown in Fig. 15(a), which indirectly indicates that easiness of cracking around the notch tip. Here note that the strain rate effect discussed in the previous section implies the importance of cohesive energy and plasticity-induced damage at grain boundaries. In this regard, hydrogen has been reported to assist decohesion [51,52] and plasticity-induced

damage localization [24,33,53] at grain boundaries. In Fig. 15, both brittle-like sharp crack tip and plasticity-driven dislocation microstructure evolution were observed near the fracture surface. Furthermore, localization of plastic strain near grain boundaries was also observed in the hydrogen-charged specimen (Fig. 12) similar to the case without hydrogen charging (Figs. 10 and 11); however, the absolute amounts of dislocation and twin were observed to be lower than the cases without hydrogen charging (Figs. 13–15). To these ends, macroscopic strain for failure is different but local strain for failure is similar for hydrogen-charged and uncharged specimens as fracture displacement for hydrogen-charged specimen is smaller than uncharged specimen whereas strain localization near the fracture surface is similar. These facts indicate that the primary effect of hydrogen is a reduction in cohesive energy for intergranular fracture, and hydrogen-related localized plasticity effect is the second factor. On the other hand, for the quasi-cleavage fracture that was only rarely observed in the uncharged specimen, hydrogen-assisted plasticity-induced damage evolution would play an important role. In general, brittle-like transgranular crack growth in austenitic steels requires plasticity-induced precursor such as defected incoherent twin boundary [54], planar dislocation array [55,56], and cell wall [57], otherwise, there is no reason for the brittle-like cracking in grain interior. Therefore, in case of the quasi-cleavage cracking observed in Fig. 9(c, e) must be caused by hydrogen-related plastic damage evolution primarily. Then, hydrogen localization at the plastically damaged region (e.g, dislocation arrays) can cause the brittle-like quasi-cleavage fracture.

Conclusions

The effects of strain rate and hydrogen on crack growth from a notch in Fe-33Mn-1.1C steel subjected to cross head displacement speeds of 10^{-2} and 10^{-4} mm/s during tensile test were investigated. On the basis of the obtained results, the following conclusions were drawn:

1 Decreasing cross head displacement speed degraded the elongation even without hydrogen charging. The reduction in elongation was mainly due to the occurrence of intergranular crack initiation at low cross head displacement speed. The driving forces for intergranular cracking in the studied steel were dislocation-carbon interactions and corresponding dynamic strain aging (DSA) and plasticity-driven damage along grain boundaries. The increase in crack tip stress level associated with stress triaxiality also led to early crack initiation from notch at the lower cross head displacement speed. The fracture mode changed from ductile dimple like to brittle intergranular at low cross head speed. However, the crack propagation path was not affected by the cross head speed and found to occur mainly along the grain boundary.
2 With the introduction of hydrogen, the yield strength as well as the elongation degraded significantly. The decrease in yield was attributed to crack initiation at the notch tip before apparent yielding. The crack propagation path, along the grain boundary, was not affected by the hydrogen charging. However, brittle-like sharp crack tips were observed in hydrogen charged specimen.
3 Transportation of hydrogen to the grain boundaries during deformation resulted in the lowering of the cohesive energy for intergranular fracture by HEDE mechanism. The lowering of the cohesive energy together with the hydrogen-related localized plasticity effect resulted in intergranular fracture and lead to deterioration in the elongation for the hydrogen charged specimen.

Acknowledgements

This work was financially supported by the Japan Science and Technology Agency (JST) (grant number: 20100113) under the Industry-Academia Collaborative R&D Program and JSPS KAKENHI (JP16H06365 and JP17H04956). B. Bal acknowledges the Scientific and Technological Research Council of Turkey (TÜBİTAK, Project No: 118M448).

REFERENCES

[1] Lee S-J, Kim J, Kane SN, De Cooman BC. On the origin of dynamic strain aging in twinning-induced plasticity steels. Acta Mater 2011;59:6809–19. https://doi.org/10.1016/J.ACTAMAT.2011.07.040.
[2] Bal B, Gumus B, Gerstein G, Canadinc D, Maier HJ. On the micro-deformation mechanisms active in high-manganese austenitic steels under impact loading. Mater Sci Eng A 2015;632. https://doi.org/10.1016/j.msea.2015.02.054.
[3] Gumus B, Bal B, Gerstein G, Canadinc D, Maier HJ. Twinning activity in high-manganese austenitic steels under high velocity loading. Mater Sci Technol 2016;32:463–5. https://doi.org/10.1179/1743284715Y.0000000111.
[4] Koyama M, Sawaguchi T, Lee T, Lee CS, Tsuzaki K. Work hardening associated with ϵ-martensitic transformation, deformation twinning and dynamic strain aging in Fe–17Mn–0.6C and Fe–17Mn–0.8C TWIP steels. Mater Sci Eng A 2011;528:7310–6. https://doi.org/10.1016/j.msea.2011.06.011.
[5] Koyama M, Sawaguchi T, Tsuzaki K. Overview of dynamic strain aging and associated phenomena in Fe-Mn-C austenitic steels. Tetsu-to-Hagane 2018;104:187–200. https://doi.org/10.2355/tetsutohagane.TETSU-2017-089.
[6] Dumay A, Chateau J-P, Allain S, Migot S, Bouaziz O. Influence of addition elements on the stacking-fault energy and mechanical properties of an austenitic Fe–Mn–C steel. Mater Sci Eng A 2008;483–484:184–7. https://doi.org/10.1016/J.MSEA.2006.12.170.
[7] Perng TP, Altstetter CJ. Comparison of hydrogen gas embrittlement of austenitic and ferritic stainless steels. Metall Trans A 1987;18:123–34. https://doi.org/10.1007/BF02646229.
[8] Hirata K, Iikubo S, Koyama M, Tsuzaki K, Ohtani H. First-principles study on hydrogen diffusivity in BCC, FCC, and HCP iron. Metall Mater Trans A 2018;49:5015–22. https://doi.org/10.1007/s11661-018-4815-9.
[9] Li Y-F, Zhao L-M, Pan H-L. Hydrogen permeation behaviour and associated phase transformations in annealed AISI304 stainless steels. Mater Struct 2013;46:621–7. https://doi.org/10.1617/s11527-012-9920-4.

[10] Chun YS, Lee J, Bae CM, Park K-T, Lee CS. Caliber-rolled TWIP steel for high-strength wire rods with enhanced hydrogen-delayed fracture resistance. Scr Mater 2012;67:681–4. https://doi.org/10.1016/J.SCRIPTAMAT.2012.07.006.
[11] Tsuzaki K, Fukuda K, Koyama M, Matsunaga H. Hexagonal close-packed martensite-related fatigue crack growth under the influence of hydrogen: example of Fe–15Mn–10Cr–8Ni–4Si austenitic alloy. Scr Mater 2016;113:6–9. https://doi.org/10.1016/J.SCRIPTAMAT.2015.10.016.
[12] San Marchi C, Somerday BP, Tang X, Schiroky GH. Effects of alloy composition and strain hardening on tensile fracture of hydrogen-precharged type 316 stainless steels. Int J Hydrogen Energy 2008;33:889–904. https://doi.org/10.1016/J.IJHYDENE.2007.10.046.
[13] Mittal SC, Prasad RC, Deshmukh MB. Effect of hydrogen on fracture of austenitic Fe-Mn-Al steel. ISIJ Int 1994;34:211–6. https://doi.org/10.2355/isijinternational.34.211.
[14] Koyama M, Akiyama E, Tsuzaki K. Hydrogen embrittlement in a Feâ€“Mnâ€“C ternary twinning-induced plasticity steel. Corros Sci 2012;54:1–4. https://doi.org/10.1016/j.corsci.2011.09.022.
[15] Koyama M, Akiyama E, Lee Y-K, Raabe D, Tsuzaki K. Overview of hydrogen embrittlement in high-Mn steels. Int J Hydrogen Energy 2017;42:12706–23. https://doi.org/10.1016/J.IJHYDENE.2017.02.214.
[16] Koyama M, Springer H, Merzlikin SV, Tsuzaki K, Akiyama E, Raabe D. Hydrogen embrittlement associated with strain localization in a precipitation-hardened Fe–Mn–Al–C light weight austenitic steel. Int J Hydrogen Energy 2014;39:4634–46. https://doi.org/10.1016/J.IJHYDENE.2013.12.171.
[17] Chun YS, Park K-T, Lee CS. Delayed static failure of twinning-induced plasticity steels. Scr Mater 2012;66:960–5. https://doi.org/10.1016/J.SCRIPTAMAT.2012.02.038.
[18] Dwivedi SK, Vishwakarma M. Hydrogen embrittlement in different materials: a review. Int J Hydrogen Energy 2018;43:21603–16. https://doi.org/10.1016/J.IJHYDENE.2018.09.201.
[19] Zhou C, Ye B, Song Y, Cui T, Xu P, Zhang L. Effects of internal hydrogen and surface-absorbed hydrogen on the hydrogen embrittlement of X80 pipeline steel. Int J Hydrogen Energy 2019;44:22547–58. https://doi.org/10.1016/J.IJHYDENE.2019.04.239.
[20] Robertson IM. The effect of hydrogen on dislocation dynamics. Eng Fract Mech 2001;68:671–92. https://doi.org/10.1016/S0013-7944(01)00011-X.
[21] Depover T, Verbeken K. The detrimental effect of hydrogen at dislocations on the hydrogen embrittlement susceptibility of Fe-C-X alloys: an experimental proof of the HELP mechanism. Int J Hydrogen Energy 2018;43:3050–61. https://doi.org/10.1016/j.ijhydene.2017.12.109.
[22] Dwivedi SK, Vishwakarma M. Effect of hydrogen in advanced high strength steel materials. Int J Hydrogen Energy 2019;44:28007–30. https://doi.org/10.1016/j.ijhydene.2019.08.149.
[23] Martínez-Pañeda E, Golahmar A, Niordson CF. ScienceDirect A phase field formulation for hydrogen assisted cracking. 2018. https://doi.org/10.1016/j.cma.2018.07.021.
[24] Mohammadi A, Koyama M, Gerstein G, Maier HJ, Noguchi H. Hydrogen-assisted failure in a bimodal twinning-induced plasticity steel: delamination events and damage evolution. Int J Hydrogen Energy 2018;43:2492–502. https://doi.org/10.1016/j.ijhydene.2017.11.177.
[25] Lan P, Tang H, Zhang J. Hot ductility of high alloy Fe–Mn–C austenite TWIP steel. Mater Sci Eng A 2016;660:127–38. https://doi.org/10.1016/J.MSEA.2016.02.086.
[26] Chen S, Rana R, Haldar A, Ray RK. Current state of Fe-Mn-Al-C low density steels. Prog Mater Sci 2017;89:345–91. https://doi.org/10.1016/J.PMATSCI.2017.05.002.
[27] Chowdhury P, Canadinc D, Sehitoglu H. On deformation behavior of Fe-Mn based structural alloys. Mater Sci Eng R Rep 2017;122:1–28. https://doi.org/10.1016/J.MSER.2017.09.002.
[28] Yang HK, Tian YZ, Zhang ZF. Revealing the mechanical properties and microstructure evolutions of Fe–22Mn–0.6C–(x)Al TWIP steels via Al alloying control. Mater Sci Eng A 2018;731:61–70. https://doi.org/10.1016/J.MSEA.2018.06.037.
[29] Zhang L, Wen M, Imade M, Fukuyama S, Yokogawa K. Effect of nickel equivalent on hydrogen gas embrittlement of austenitic stainless steels based on type 316 at low temperatures. Acta Mater 2008;56:3414–21. https://doi.org/10.1016/J.ACTAMAT.2008.03.022.
[30] Koyama M, Akiyama E, Tsuzaki K. Effects of static and dynamic strain aging on hydrogen embrittlement in TWIP steels containing Al. Tetsu-to-Hagane 2014;100:1132–9. https://doi.org/10.2355/tetsutohagane.100.1132.
[31] Ogawa T, Koyama M, Tasan CC, Tsuzaki K, Noguchi H. Effects of martensitic transformability and dynamic strain age hardenability on plasticity in metastable austenitic steels containing carbon. J Mater Sci 2017;52:7868–82. https://doi.org/10.1007/s10853-017-1052-3.
[32] Dai YJ, Li B, Ma HE, Zhang C. Influence of carbon on the stacking fault energy and deformation mechanics of Fe-Mn-C system Alloys. Appl Mech Mater 2015;710:9–14. https://doi.org/10.4028/www.scientific.net/AMM.710.9.
[33] Tuğluca IB, Koyama M, Bal B, Canadinc D, Akiyama E, Tsuzaki K. High-concentration carbon assists plasticity-driven hydrogen embrittlement in a Fe-high Mn steel with a relatively high stacking fault energy. Mater Sci Eng A 2018;717:78–84. https://doi.org/10.1016/j.msea.2018.01.087.
[34] Tuğluca IB, Koyama M, Shimomura Y, Bal B, Canadinc D, Akiyama E, et al. Lowering strain rate simultaneously enhances carbon- and hydrogen-induced mechanical degradation in an Fe-33Mn-1.1C steel. Metall Mater Trans A 2019:1–5. https://doi.org/10.1007/s11661-018-5080-7.
[35] Ryu JH, Kim SK, Lee CS, Suh DW, Bhadeshia HKDH. Effect of aluminium on hydrogen-induced fracture behaviour in austenitic Fe-Mn-C steel. Proc R Soc A Math Phys Eng Sci 2013;469. https://doi.org/10.1098/rspa.2012.0458.
[36] Koyama M, Akiyama E, Tsuzaki K, Raabe D. Hydrogen-assisted failure in a twinning-induced plasticity steel studied under in situ hydrogen charging by electron channeling contrast imaging. Acta Mater 2013;61:4607–18. https://doi.org/10.1016/j.actamat.2013.04.030.
[37] Madivala M, Schwedt A, Prahl U, Bleck W. Anisotropy and strain rate effects on the failure behavior of TWIP steel: a multiscale experimental study. Int J Plast 2019;115:178–99. https://doi.org/10.1016/J.IJPLAS.2018.11.015.
[38] Hamada AS, Karjalainen LP, Puustinen J. Fatigue behavior of high-Mn TWIP steels. Mater Sci Eng A 2009;517:68–77. https://doi.org/10.1016/J.MSEA.2009.03.039.
[39] De Cooman BC, Estrin Y, Kim SK. Twinning-induced plasticity (TWIP) steels. Acta Mater 2018;142:283–362. https://doi.org/10.1016/J.ACTAMAT.2017.06.046.
[40] Kale C, Rajagopalan M, Turnage S, Hornbuckle B, Darling K, Mathaudhu SN, et al. On the roles of stress-triaxiality and strain-rate on the deformation behavior of AZ31 magnesium alloys. 2017. https://doi.org/10.1080/21663831.2017.1417923.
[41] Bintu A, Vincze G, Picu CR, Lopes AB, Grácio JJ, Barlat F. Strain hardening rate sensitivity and strain rate sensitivity in TWIP steels. Mater Sci Eng A 2015;629:54–9. https://doi.org/10.1016/J.MSEA.2015.01.080.

[42] Yang HK, Zhang ZJ, Dong FY, Duan QQ, Zhang ZF. Strain rate effects on tensile deformation behaviors for Fe–22Mn–0.6C–(1.5Al) twinning-induced plasticity steel. Mater Sci Eng A 2014;607:551–8. https://doi.org/10.1016/J.MSEA.2014.04.043.
[43] Li YZ, Luo ZC, Liang ZY, Huang MX. Effect of carbon on strain-rate and temperature sensitivity of twinning-induced plasticity steels: modeling and experiments. Acta Mater 2019;165:278–93. https://doi.org/10.1016/J.ACTAMAT.2018.11.048.
[44] Koyama M, Akiyama E, Tsuzaki K. Factors affecting static strain aging under stress at room temperature in a Fe-Mn-C twinning-induced plasticity steel. Tetsu-to-Hagane 2014;100:1123–31. https://doi.org/10.2355/tetsutohagane.100.1123.
[45] Belotteau J, Berdin C, Forest S, Parrot A, Prioul C. Mechanical behavior and crack tip plasticity of a strain aging sensitive steel. Mater Sci Eng A 2009;526:156–65. https://doi.org/10.1016/j.msea.2009.07.013.
[46] Graff S, Forest S, Strudel J-L, Prioul C, Pilvin P, Béchade J-L. Finite element simulations of dynamic strain ageing effects at V-notches and crack tips. Scr Mater 2005;52:1181–6. https://doi.org/10.1016/J.SCRIPTAMAT.2005.02.007.
[47] Seo W, Jeong D, Sung H, Kim S. Tensile and high cycle fatigue behaviors of high-Mn steels at 298 and 110 K. Mater Char 2017;124:65–72. https://doi.org/10.1016/J.MATCHAR.2016.12.001.
[48] Mejía I, Salas-Reyes AE, Calvo J, Cabrera JM. Effect of Ti and B microadditions on the hot ductility behavior of a High-Mn austenitic Fe–23Mn–1.5Al–1.3Si–0.5C TWIP steel. Mater Sci Eng A 2015;648:311–29. https://doi.org/10.1016/J.MSEA.2015.09.079.
[49] Koyama M, Shimomura Y, Chiba A, Akiyama E, Tsuzaki K. Room-temperature blue brittleness of Fe-Mn-C austenitic steels. Scr Mater 2017;141:20–3. https://doi.org/10.1016/j.scriptamat.2017.07.017.
[50] Koyama M, Akiyama E, Sawaguchi T, Raabe D, Tsuzaki K. Hydrogen-induced cracking at grain and twin boundaries in an Fe–Mn–C austenitic steel. Scr Mater 2012;66:459–62. https://doi.org/10.1016/J.SCRIPTAMAT.2011.12.015.
[51] Wan L, Geng WT, Ishii A, Du J-P, Mei Q, Ishikawa N, et al. Hydrogen embrittlement controlled by reaction of dislocation with grain boundary in alpha-iron. Int J Plast 2019;112:206–19. https://doi.org/10.1016/J.IJPLAS.2018.08.013.
[52] Nagao A, Dadfarnia M, Somerday BP, Sofronis P, Ritchie RO. Hydrogen-enhanced-plasticity mediated decohesion for hydrogen-induced intergranular and "quasi-cleavage" fracture of lath martensitic steels. J Mech Phys Solids 2018;112:403–30. https://doi.org/10.1016/J.JMPS.2017.12.016.
[53] Maier HJ, Popp W, Kaesche H. Effects of hydrogen on ductile fracture of a spheroidized low alloy steel. Mater Sci Eng A 1995;191:17–26. https://doi.org/10.1016/0921-5093(94)09623-5.
[54] Zheng L, Hu X, Kang X, Li D. Precipitation of M23C6 and its effect on tensile properties of 0.3C–20Cr–11Mn–1Mo–0.35N steel. Mater Des 2015;78:42–50. https://doi.org/10.1016/j.matdes.2015.04.016.
[55] Astafurova EG, Moskvina VA, Maier GG, Gordienko AI, Burlachenko AG, Smirnov AI, et al. Low-temperature tensile ductility by V-alloying of high-nitrogen CrMn and CrNiMn steels: characterization of deformation microstructure and fracture micromechanisms. Mater Sci Eng A 2019;745:265–78. https://doi.org/10.1016/j.msea.2018.12.107.
[56] Zhou H, He Y, Cui M, Cen Y, Jiang J. Dependence of dynamic strain ageing on strain amplitudes during the low-cycle fatigue of TP347H austenitic stainless steel at 550 °C. Int J Fatigue 2013;56:1–7. https://doi.org/10.1016/J.IJFATIGUE.2013.07.010.
[57] Sadananda K, Nani Babu M, Vasudevan AK. A review of fatigue crack growth resistance in the short crack growth regime. Mater Sci Eng A 2019;754:674–701. https://doi.org/10.1016/J.MSEA.2019.03.102.